

New CMB Power Spectrum Constraints from MSAM1

G. W. Wilson^{1,2}, L. Knox¹, S. Dodelson³, K. Coble¹,
E. S. Cheng², D. A. Cottingham⁴, D. J. Fixsen⁵,
A. B. Goldin¹, C. A. Inman⁶, M. S. Kowitt⁶, S. S. Meyer¹,
L. A. Page⁷, J. L. Puchalla⁸, J. E. Ruhl⁹, and R. F. Silverberg²

Abstract

We present new cosmic microwave background (CMB) anisotropy results from the combined analysis of the three flights of the first Medium Scale Anisotropy Measurement (MSAM1). This balloon-borne bolometric instrument measured about 10 square degrees of sky at half-degree resolution in 4 frequency bands from 5.2 cm^{-1} to 20 cm^{-1} with a high signal-to-noise ratio. Here we present an overview of our analysis methods, compare the results from the three flights, derive new constraints on the CMB power spectrum from the combined data and reduce the data to total power Wiener-filtered maps of the CMB. A key feature of this new analysis is a determination of the amplitude of CMB fluctuations at $\ell \sim 400$. The analysis technique is described in a companion paper (Knox 1999).

Subject headings: balloons — cosmic microwave background — cosmology: observations — infrared: ISM: continuum

1. Introduction

The Medium Scale Anisotropy Measurement (MSAM) is a balloon-borne telescope and bolometric radiometer designed to measure the anisotropy in the cos-

mic microwave background (CMB) at angular scales near 0.5° . The first two flights of MSAM1, reported in (Cheng *et al.* 1994) (MSAM92) and (Cheng *et al.* 1996) (MSAM94), observed overlapping fields on the sky and demonstrated the repeatability of the measurement. A detailed comparison, showing consistency between these two flights, was reported in (Inman *et al.* 1997) and (Knox *et al.* 1998). A third flight (Cheng *et al.* 1997) (MSAM95) measured a nearby region of sky using the same observing method. This increased the experimental sky coverage and sensitivity to the CMB anisotropy power spectrum. A second version of this instrument (MSAM II) with complementary frequency coverage has since been flown. This data set is still being analyzed.

2. Instrument and Observations

The MSAM1 instrument is described in (Fixsen *et al.* 1996). We give a summary here. The actively pointed gondola is composed of a 1.4 m off-axis Cassegrain telescope with a multimode bolometric radiometer. A three-position chopping secondary throws the frequency independent $\sim 0.5^\circ$ primary beam $\pm 0.7^\circ$ tangent to the local horizon at 2 Hz. The four spectral channels at 5.7, 9.3, 16.5, and 22.5 cm^{-1} , each have bandwidth of $\sim 1.5 \text{ cm}^{-1}$. The detectors' outputs are synchronously sampled at 32 Hz: 4 times for each of 4 positions of the secondary mirror, for a total of 16 samples per chopper cycle. Telescope pointing is controlled with a star camera and gyroscope. The configuration of the gondola superstructure was changed between the 92 and 94 flights to reduce possible reflection of ground radiation. The improved configuration remained for MSAM95.

All three flights were launched from the National Scientific Balloon Facility in Palestine, Texas. The observing method, also described in (Fixsen *et al.* 1996), is a slow azimuth scan of a region crossing the meridian above the North Celestial Pole. For a period of 20 minutes the scan center tracks a fixed spot on the sky as the earth rotates. Afterwards, an overlapping region is scanned. MSAM92 and MSAM94 observed at declination $\delta = +82^\circ 0'$, MSAM95 at $\delta = +80^\circ 5'$. The flights observed between right ascensions $14^{\text{h}} 2'$ and $19^{\text{h}} 5'$. The lower declination of the MSAM95 required a faster scan rate because of the increased sky motion. The sky coverage of all the MSAM1 flights

¹University of Chicago, 5640 S. Ellis Ave., Chicago, IL 60637

²NASA/Goddard Space Flight Center, Laboratory for Astronomy and Solar Physics, Code 685.0, Greenbelt, MD 20771

³Fermilab, P.O. Box 500, Batavia, IL 60510

⁴Global Science and Technology, Inc., NASA/GSFC Laboratory for Astronomy and Solar Physics, Code 685.0, Greenbelt, MD 20771

⁵Applied Research Corporation, NASA/GSFC Laboratory for Astronomy and Solar Physics, Code 685.0, Greenbelt, MD 20771

⁶Stanford Research Systems, Sunnyvale, CA 94089

⁷Princeton University, Princeton, NJ 08544

⁸Department of Physics and Astronomy, University of Pennsylvania, Philadelphia, PA 19104

⁹University of California at Santa Barbara, Santa Barbara, CA 93106

is shown in Fig. 1.

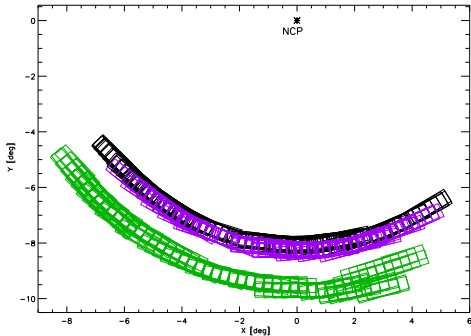


Fig. 1.— Locations in the data file (flat) sky coordinates for the 1010 MSAM1 points. The boxes show the relative twist of the beam-pattern during the observation. The upper row of points come from the overlapping flights, two years apart, of MSAM92 and MSAM94. The lower row are the MSAM95 points.

3. Data Reduction

The data from each of the three flights of MSAM1 are independently reduced in the same manner. A detailed discussion of the analysis for each of the three flights is available in (Cheng *et al.* 1994, Cheng *et al.* 1996, Cheng *et al.* 1997) respectively. We outline the process here.

1) Spikes caused by cosmic rays are removed from the time stream by a filtering and peak detecting technique which results in the deletion of 5% to 10% of the data. Samples are also lost due to spurious electrical pickup and telemetry dropouts. For each of these cuts, a full chopper cycle is deleted. The total loss is between 10 and 30% of the raw data.

2) The detector time streams are demodulated in two ways – each resulting in an independent instrumental beam pattern and corresponding instrumental window function. If T_L , T_C , and T_R are the sky temperature at the left, center, and right position of the beam during a chopper cycle, the single difference demodulation is $T_R - T_L$, making an antisymmetric beam pattern, while the double difference is $T_C - (T_L + T_R)/2$, making a symmetric beam-pattern. Optimum weighting for the demodulations are determined from Jupiter observations. The instrument noise is uncorrelated between between the two demodulations.

3) The data are calibrated using scan and raster

observations of Jupiter. The brightness temperature of Jupiter is reported in (Goldin *et al.* 1997). Of the two models presented in that paper, we use the temperatures based on the “Rudy” model (Rudy *et al.* 1987). The error in the calibration is estimated to be 5%, dominated by the uncertainty in the Jupiter temperature.

4) The Jupiter raster observations, performed during each flight, are the basis for the high fidelity determination of the beam pattern for each demodulation. Beam-pattern uncertainties are dominated by arcminute-scale pointing uncertainties.

5) The estimate of the instrument noise is determined from the variance in 100 s segments of the demodulated data after the removal of a slowly drifting offset. The offset ranges from 1 to 6 mK in MSAM94 and MSAM95 with an offset of 10 mK R-J in all channels in MSAM92. The drift in the offset is small compared to its value. Because the removal of the offset correlates the noise on time scales longer than the detector time constant, the remainder of the data reduction incorporates the *full* noise covariance matrix.

6) The data are binned according to both the position on the sky and the twist of the demodulated beam pattern during each complete chopper cycle. The bin size for the twist dimension is determined by defining a “Binning Degradation Factor,” $BDF = \sqrt{\sigma^2 + \langle \delta^2 \rangle} / \sigma$ where σ is the estimated instrument noise and $\langle \delta^2 \rangle = \int (|B_1(\vec{k}) - B_2(A\vec{k})|^2 C_{\text{cdm}}(\vec{k})) d\vec{k}$ is an estimate of the expected error in the estimate of the signal due to the twist bin size. $\langle \delta^2 \rangle$ is determined using the standard cold dark matter correlation function $C_{\text{cdm}}(\vec{k})$ convolved with beam-patterns, $B_i(\vec{k})$ twisted with respect to each other by the rotation matrix A . A similar construction is used to define the BDF for the spatial binning. The BDF can be thought of as the factor by which the sensitivity of the data set is decreased due to the choice of bin size. The bin sizes are chosen to hold the BDF to values less than 1.1. This results in 5° twist bins and 14' bins in sky position.

7) The calibrated data are analyzed to provide measurements of brightness in the four spectral channels as a function of bin. The linear combination of the spectral channels which minimizes the sensitivity of galactic dust foreground and matches the signature of a CMB thermal fluctuation over the spectral range of the instrument channels is found and an estimate of

CMB anisotropy and dust optical depth for each bin is produced. This is done by fitting the data for each bin in the four channels to a two parameter model of sky and dust.

4. Comparison of MSAM92 and MSAM94

The overlapping regions of MSAM92 and MSAM94 (see Fig. 1) are used to compare their estimated sky signals. This can place a limit on how much of the signal could be attributed to instrumental artifacts or other local contamination. While straightforward in principle, a simple comparison is not possible despite the large degree of overlap. The beam centers for each sample do not line up perfectly and because of the twist dimension in the binning, there are few bins that are populated in both flights. In (Inman *et al.* 1997) the bin size was expanded over the criterion in the previous section and those bins with sufficient data were differenced. With rather reduced sky coverage, (Inman *et al.* 1997) found no signal in the differenced data.

An alternative procedure for comparing the two measurements has been previously reported in (Knox *et al.* 1998). Here, an assumed power spectrum for the CMB fluctuations is used to make a prediction of the most likely signal in the 1992 data set, given the 1992 pointing information. This is compared to the most likely value of the signal in the same 1992 data set but given the 1994 pointings. This “most likely” signal is determined by applying a Wiener filter to the data. See (Knox *et al.* 1998) for details. In Fig. 2 we see that the two data sets predict very similar signals for the 1992 data set using either the 1992 or 1994 data.

We quantify “very similar” by use of the likelihood ratio statistic. The two hypotheses are 1) the signals are correlated as one would expect (given the two sampling strategies and an assumed power spectrum) and 2) the signals are uncorrelated between data sets. We use the natural log of the likelihood ratio statistic, which is a quadratic operator on the data denoted by β ¹. For the 1992 and 1994 data sets (Knox *et al.* 1998) has found $\beta = 12.8$, which means that hypothesis 1 is $e^{12.8}$ times more likely than hypothesis 2. A frequentist interpretation of β is given by calculating the expected mean and standard deviation of the statistic under the different hypotheses. The result is

¹Also see (Tegmark 1998) on the optimization of quadratic comparison statistics.

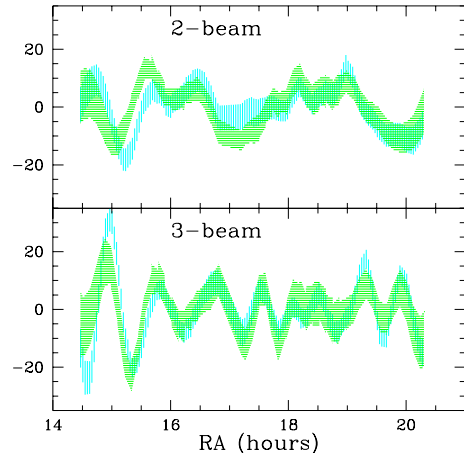


Fig. 2.— Most likely signal in 1992 data set, given the COBE-normalized standard CDM power spectrum and the 1992 data (vertical lines) or the 1994 data (horizontal lines). The shaded area is the 68% confidence region. Single-difference (or “2-beam”) data in top panel, double-difference (or “3-beam”) in the bottom panel.

15.0 ± 4.1 (hypothesis 1) and -58.4 ± 27.4 (hypothesis 2). This analysis is in agreement with (Inman *et al.* 1997) that it is extremely unlikely that the data sets are caused by a signal that is uncorrelated between experiments. Based on these analyses, we conclude that the signal comes from the sky and not from the instrument or local environment.

5. Likelihood Analysis

The data set from the three flights of MSAM has been reduced to 505 measurements of the CMB sky, for each of the two demodulations. We model this data, d as due to signal and noise

$$d_i = s_i + n_i \quad (1)$$

where i runs from 1 to 505 over the single-difference demodulation and from 506 to 1010 over the double-difference demodulation, and the signal, s , is related to the true temperature field, T , by

$$s_i = \int_{\Omega} B(\vec{x} - \vec{x}_i) T(\vec{x}) d\vec{x}. \quad (2)$$

Here, $B(\vec{x})$ is the (single or double difference) beammap, and \vec{x}_i specifies the pointing. We assume that both the signal and noise are Gaussian-distributed with

zero mean with covariance matrices which we denote by $S_{ij} = \langle s_i s_j \rangle$ and $N_{ij} = \langle n_i n_j \rangle$.

The noise covariance matrix, N , is block-diagonal with each block representing the noise correlations of a single demodulation from a single flight. The noise covariance matrix is singular due to the independent offset removals from each of the three flights (two each in MSAM92 and MSAM94). This constraint must be explicitly projected out of the data which we do with an SVD inversion of N .

The signal covariance matrix is linearly related to the angular power spectrum of the temperature field, C_l . The likelihood of this power spectrum, given the data, noise matrix and our assumptions of Gaussianity is

$$L(C_l) = \frac{e^{-\frac{1}{2} \vec{d} C^{-1} \vec{d}^T}}{(2\pi)^{N/2} \sqrt{\det C}} \quad (3)$$

where \vec{d} is the n -element vector of observations and $C = [S(C_l) + N]$ is the $(n \times n)$ covariance matrix of the observations. We use this likelihood to place limits on the power spectrum of fluctuations.

For this analysis we parameterize the theoretical signal covariance matrix, S , with the power spectrum, $C_l \equiv l(l+1)C_l/(2\pi)$, broken into bands denoted by B so that

$$C_l = \sum_B \chi_{B(l)} C_B, \quad (4)$$

where C_B denotes is a flat power spectrum within band B with amplitude C_B . That is,

$$C_B = \frac{l(l+1)}{2\pi} C_B. \quad (5)$$

The sum runs over the bands in l -space with

$$\chi_{B(l)} = \begin{cases} 1 & : l_{<}(B) < l < l_{>}(B) \\ 0 & : \text{otherwise} \end{cases} \quad (6)$$

This parameterization of C_l is completely general and its usefulness will become apparent below.

The calculation of the likelihood requires the inversion of the $(n \times n)$ covariance matrix C . It has been shown in (Bond 1994, Tegmark, Taylor, and Heavens 1996, Bunn and White 1997, Bond and Jaffe 1997) that a substantial reduction in the rank of C can be achieved by working in the signal-to-noise eigenmode basis. This is true even in a high signal-to-noise case like that of MSAM1. For this data set, we achieve a compression by a factor of 1.8 in the rank of C by ignoring modes with signal-to-noise ratio of less than

0.03. Working in the signal-to-noise eigenmode basis has the added benefit of automatically projecting out the eigenmodes associated with the offset removal. Thus, only one initial SVD of the covariance matrix is required (to zero the infinite eigenvalues). Inversions of the covariance matrix in the signal-to-noise eigenmode basis are then done using faster methods such as Cholesky decomposition.

6. The Flat Band-Power

As has been done previously for each of the data sets individually (Cheng *et al.* 1994, Cheng *et al.* 1996, Cheng *et al.* 1997), we calculate “flat band-powers” for each demodulation. That is, we assume the entire power spectrum is flat with amplitude $C_l = C_B$ and calculate the likelihood of this amplitude. Table 1 gives the flat band-powers (maximum likelihood values of $\sqrt{C_B}$) for the three flights of MSAM1 for the single and double difference demodulations. The error bars indicate where the likelihood falls to $e^{-1/2}$ of the maximum.

Flight	Single Diff.	Double Diff.
MSAM92	48 ± 11	54 ± 10
MSAM94	35 ± 6	45 ± 9
MSAM95	51 ± 7	56 ± 7
all three	47 ± 5	53 ± 5

Table 1: Flat Band-power Estimates for MSAM1 in μK

7. Radical Compression

Flat band-powers, together with the diagonal parts of the window function matrix, often simply called the window function, have traditionally been the main results of CMB experiments. When taken together, they are the raw ingredients for constraining the power spectrum and cosmological parameters.

The parameters, a_p , are found by minimizing the χ^2 where

$$\chi^2 = \sum_B \left(\sum_l f_{Bl} C_l(a_p) - C_B \right)^2 / \sigma_B^2, \quad (7)$$

where B runs over different data sets, C_B and σ_B are the band-powers and their standard errors respectively, and f_{Bl} is a filter which, when summed over the power spectrum, C_l , gives the theoretical prediction for the band-power, C_B . The filter is usually

constructed from the familiar window function, W_{Bl}

$$f_{Bl} = \frac{W_{Bl}/l}{\sum W_{Bl}/l}. \quad (8)$$

We call the filter given by this equation the window function filter. The parameters a_p could be cosmological parameters (e.g., Ω_b , Ω_Λ , H_0 , etc.) or parameters from a phenomenological power spectrum.

7.1. Problems With Flat Band Powers ...

Using flat band-powers as a form of radical compression has the following drawbacks:

1. The actual sky power spectrum is not flat.
2. The expectation value of the band power is not given by summing the window function filter over the power spectrum, and thus the window function filter should not be used in Eq. 7. The expectation value is only given by this sum in the limit that the data points have no signal correlations.
3. The method provides no estimate of the correlation between the errors in the estimates of \mathcal{C}_B from different demodulations.
4. The constraints on the parameters are not Gaussian, even though this assumption is implicit in the χ^2 minimization.

Problems 1 and 3 are well known deficiencies of the bandpower approach. Problem 4 has been emphasized in (Bond, Jaffe, and Knox 1998b), where an approximate solution was given. Here we focus on problem 2, which has been discussed previously in (Bond, Jaffe, and Knox 1998a). We illustrate the potential severity of the problem with an extreme example. Consider a total power mapping experiment with angular resolution of FWHM = 30' which has measured a $5^\circ \times 5^\circ$ patch of the sky. The window function filter for this experiment is $f_l \propto W_l/l = \exp(-l^2\sigma_b^2)/l$ where $\sigma_b \simeq \text{FWHM}/2.355$. Note that this filter peaks at $l = 0$ indicating that the experiment is most sensitive to fluctuations on very large angular scales. However, the data set is not actually sensitive to the lowest spatial frequencies at all. The problem lies in having ignored the off-diagonal terms. The filter function actually makes sense only if the data points are all far apart on the sky so that S_{ij} is diagonal. For the example given, correlations between the points on the sky

are making the data set insensitive to fluctuations on large scales. Because using the diagonal component of the window function to define the filter ignores these correlations, we get a nonsensical result. For most actual data sets, the problem is not quite so severe but this example illustrates the potential pitfall.

7.2. ... and Solutions

Solutions have been found to all of these problems (Bond, Jaffe, and Knox 1998a, Bond, Jaffe, and Knox 1998b, Knox 1999). Here we briefly review them.

Problem 1 can be solved by breaking the power spectrum into several bands as in Eq. 4, and then finding the amplitudes of these bands, \mathcal{C}_B , that maximize the likelihood. We find this maximum by iterative application of a quadratic estimator, as has been done for COBE/DMR (Bennett *et al.* 1996) and Saskatoon (Netterfield *et al.* 1997) data in (Bond, Jaffe, and Knox 1998a) and on simulated MAP data in (Oh, Spergel, and Hinshaw 1999). By calculating the covariance matrix of the set of \mathcal{C}_B we also solve problem 3.

Because physical power spectra are not actually flat across these bands, we need a means of taking a general power spectrum, \mathcal{C}_l , and turning it into a prediction for \mathcal{C}_B . In other words, we need to be able to calculate the expectation value of \mathcal{C}_B , $\langle \mathcal{C}_B \rangle$, under the assumption that the power spectrum is \mathcal{C}_l . This relationship is specified by the filter function,

$$\langle \mathcal{C}_B \rangle = f_{Bl}\mathcal{C}_l. \quad (9)$$

Taking Eq. 9 as the definition of the filter, (Knox 1999) has shown how it can be calculated from the signal and noise covariance matrices and the derivatives of S with respect to \mathcal{C}_l . Taking into account all off-diagonal terms, this prescription for f_{Bl} solves problem 2. To distinguish it from the usual practice of simply using the window function filter, we call this the minimum-variance filter. They are identical only in the limit of no signal correlations.

We could remove the need for filters by making the bands very narrow since sufficiently narrow bands ensure that the sensitivity to each \mathcal{C}_l within the band is approximately independent of l . However, making the bands too narrow would increase the non-Gaussianity – exasperating problem 4 – because the likelihood of more tightly constrained broad bands is better approximated by a Gaussian. Therefore, the bands must be broad enough to have significant constraints on

their amplitudes. For MSAM, this condition makes the bands sufficiently broad that the sensitivity to \mathcal{C}_l varies significantly across the bands, necessitating the use of a separate filter for each band.

Finally, if we adopt the (Bond, Jaffe, and Knox 1998a) prescription for problem 4, which requires calculation of a “log-normal offset”, x_B , for each \mathcal{C}_B , we have solutions to all four problems. Although these solutions are not exact, they do represent a significant improvement over the usual flat band-power method.

It is not necessary to break the power spectrum into bands to obtain parameter estimates from the observations. However, this approach aids the comparison of different experiments with a minimum of theoretical assumptions, as well as easing the comparison of experimental results with theory. By following the above procedure for power spectrum estimation, the full weight of an experiment is made available in an easily-tractable form for the kind of parameter estimation outlined in Eq. 7

7.3. The Application to MSAM I Data

The MSAM1 data sets are a prime example of the limitations of the flat band-power method. The MSAM1 data have high signal-to-noise and are heavily sample-variance limited when using standard estimators of the flat band-power. We now use the radical compression methods outlined above to probe regions of l -space ignored by our previous reduction to flat band-powers.

The difference between the minimum-variance filters, f_{Bl} , and the window function filters, is shown in Fig. 3. The plot shows the filters for each demodulation of the 3 year data for a single band covering all l . Notice that the minimum-variance filters show more response at high l than the window function filters. This is due to the fact that the dense sampling and high signal-to-noise ratio of the data set yield information on angular scales smaller than the beam size. Again, this information is in the *off-diagonal* components of the covariance matrix - underscoring the need for experiments to track the full noise covariance matrix in the data reduction.

We plot the minimum-variance filters for the individual demodulations only to make the point that they are not equal to the window-function filter as has often been assumed in the past. In the analysis we describe below, we do not treat the double-difference data sets and single-difference data sets separately;

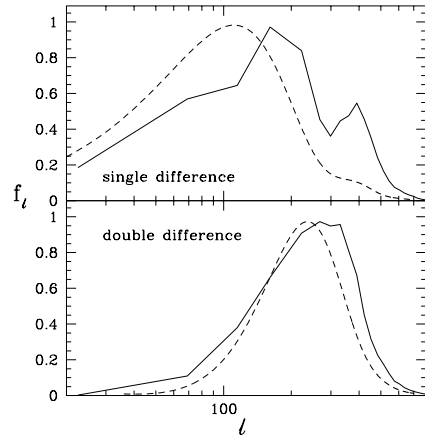


Fig. 3.— The minimum-variance filters (solid lines) and window function filters (dashed lines) for the single and double difference demodulations.

the very significant correlations between them are included.

For this analysis, we break up the l -space coverage into three wide bands and allow \mathcal{C}_B to vary in each. In line with the discussion above, we choose the three bands such that each has enough weight to produce an interesting constraint on the power spectrum. The l -ranges for the three bands chosen are 39-130, 131-283, and 284-806.

In Fig. 4 we plot the 3 power spectrum estimates, $\hat{\mathcal{C}}_B$ from the combined three years of data. The central points are located in l -space at l_{eff} which we define as the average value of l over the filter function for that band. We include a horizontal bar from l_- to l_+ . For the middle band, these are taken to be simply the beginning and end of the band ($l_- = l_< = 131$, $l_+ = l_> = 283$). For the far ends of the two outer bands, we take them to be where the filter falls to $e^{-1/2}$ of maximum. Similar results (dashed lines) are achieved by analyzing a total-power map of the CMB temperature which is constructed from the demodulated data. We take the good agreement between these two nearly independent analysis techniques as strong proof that we have calculated the complicated signal covariances correctly. We will discuss this procedure in section 8.

While the $\hat{\mathcal{C}}_B$ are not independent, their correlation coefficients are fairly small. The correlation between bands 1 and 2 is -0.18 , between bands 1 and 3 is

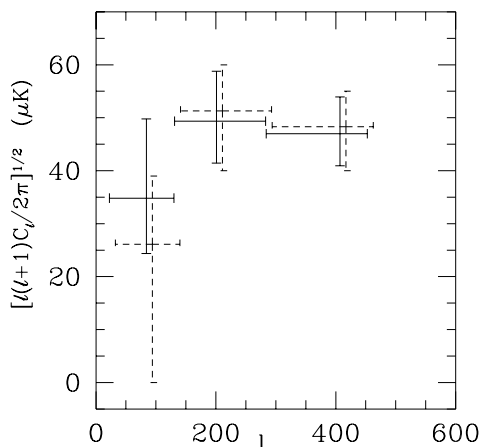


Fig. 4.— The MSAM band-power estimates. The solid lines give the estimates of the power in the three bands calculated directly from the demodulated data, and recorded in Table 2. Similar results (dashed lines) are achieved by analyzing a total-power map of the CMB temperature which is constructed from the demodulated data (see section 8).

Table 2: Power Spectrum Estimates from MSAM1

l_-	l_{eff}	l_+	$\sqrt{\hat{C}_B}$ (μK)
39	84	130	35^{+15}_{-11}
131	201	283	49^{+10}_{-8}
284	407	453	47^{+7}_{-6}

-0.024 and between bands 2 and 3 is -0.29 . The error bars shown in Fig. 4 are the result of marginalizing over the power in the other bands. Under the assumption that the other bands are fixed, the error on the band in question is less than 5 % smaller.

The power spectrum estimates, \hat{C}_B , their weight matrix, F_{ll} , filter functions, f_{Bl} , as well as log-normal offsets, x_B (see (Knox 1999)) are available at <http://topweb.gsfc.nasa.gov> and also at <http://www.cita.utoronto.ca/~knox/radical.html> which includes similar information from other CMB anisotropy data sets.

8. CMB Maps

A useful check of our power spectrum results can be made by analyzing a map made from the demodulated data as opposed to directly from the demodulated data as we have done above. We begin constructing this map by recognizing that Eq. 1 and 2 can be combined and rewritten in matrix form as

$$d = BT + n. \quad (10)$$

With the assumption that the noise is Gaussian, with covariance matrix, N , the most likely value of T , given the data, d , is that which minimizes the χ^2 :

$$\chi^2 \equiv (d - BT)N^{-1}(d - BT). \quad (11)$$

This minimum, which we denote by \hat{T} , is given by

$$\hat{T} = \tilde{N}BN^{-1}d. \quad (12)$$

This estimate of T will be distributed around the true value due to noise, where the noise covariance matrix is

$$\tilde{N} \equiv \langle (\hat{T} - T)(\hat{T} - T) \rangle = (B^T N^{-1} B)^{-1}. \quad (13)$$

This map can be analyzed in the same manner as the demodulated data, with the advantage that the signal covariance matrix is now very simple to compute. Previously, calculating the signal covariance matrix required doing a four-dimensional integral for every covariance element. In this new “map basis,” the signal covariance matrix simplifies to

$$\langle T_i T_j \rangle = \sum_l \frac{2l+1}{4\pi} P_l(\cos(\theta_{ij})) C_l. \quad (14)$$

The price to pay for this simplicity is that the noise covariance, \tilde{N} , is very complicated. We have done this

analysis as a check of the calculations in section 7.2. The results are shown in Fig. 4. The agreement is a strong argument that we have made no errors in what is a fairly elaborate and difficult calculation.

The map, \hat{T} , is extremely noisy and not visually useful. We can greatly reduce the noise by Wiener filtering, (e.g., Bunn, Hoffman, and Silk 1995, Tegmark *et al.* 1997, Knox *et al.* 1998). The Wiener filter produces the most likely T , given not only the data, but also an assumed power spectrum for the signal. The Wiener filtered maps are shown in Fig. 5.

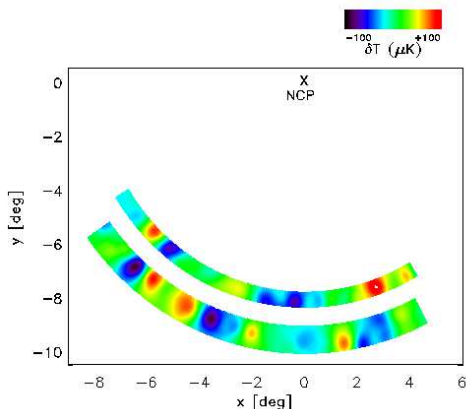


Fig. 5.— A map of the three years of data. Top region was covered by the 92/94 flight; bottom by 95 flight.

9. Discussion

Because the third band is derived by making measurements on scales on order of the beam size, we must ask what sensitivity the amplitude of \hat{C}_B has to the beam shape. For example, if the band sensitivity results from high frequency fluctuations in the measurements of the various $B_i(\vec{k})$, the estimation of the amplitude of \hat{C}_B would be suspect to the errors in determining the beammap. We address this question by performing a number of analyses of the three years of data. The first analysis (leading to the quoted values of \hat{C}_B here) is done using the six beammaps measured in the three flights. That is, MSAM92 data goes with the MSAM92 beammaps, MSAM94 data with MSAM94 beammaps, and MSAM95 data with MSAM95 beammaps. The second analysis is done using the beammaps measured during the MSAM92 flight for all three years of data. This is followed by repeating the analysis with the beammaps from

MSAM95². We find that after accounting for the normalizations of the different data sets, there is no evidence for the third band being sensitive to the beammap choice.

Reanalyzing the entire data set using beammaps measured in flight from raster observations of Jupiter for each of the three different years the experiment flew, is taken to be the most pessimistic estimator of the effect of the beam on the third band. The differences between the beammaps include all the statistical errors of the beammaps, any errors in the raster observations themselves, and any changes introduced by the complete rebuild, realignment, and refocusing of the optical system and instrument configuration.

To place our estimates of the power spectrum in context, we plot them with the predictions of several theoretical models as well as a fit of the power in 11 bands to all available data (based on (Bond, Jaffe, and Knox 1998b) including the previously published MSAM1 points.

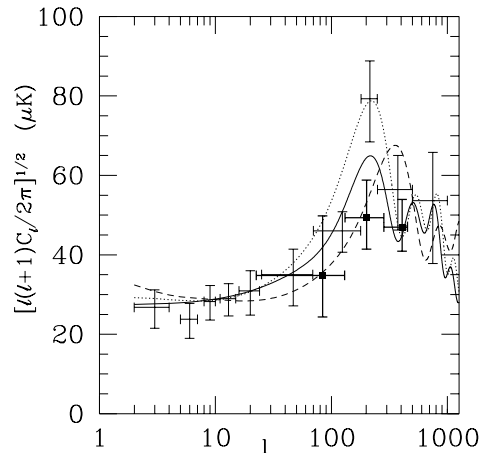


Fig. 6.— The dark error bars are the power spectrum constraints from the 3 year MSAM data set. The light error bars are the result of a fit of the power in 11 bands to all available data (based on (Bond, Jaffe, and Knox 1998b) including the previously published MSAM1 points. The curves are standard CDM (solid), a flat Lambda model (dotted), and an open model with $\Omega_{\text{curvature}} = 0.6$ (dashed).

²The MSAM92 and MSAM94 beammaps are similar enough to be swapped with no change in estimated signal.

10. Summary

We have calculated new power spectrum estimates from the combined three flights of the MSAM1 instrument. The analysis technique used is an improvement over the standard flat band-power approach and includes all correlations in the data. In addition to power-spectrum estimates and their error covariance matrices we have also provided the log-normal offsets and minimum-variance filters in order to improve “radical compression.” The analysis yields a strong constraint on the power spectrum at $l \sim 400$, broadening the l -space coverage of the experiment into a theoretically very interesting region.

This work would not be possible without the excellent support we receive from the staff of the National Scientific Balloon Facility. Financial support was provided by the NASA Office of Space Science, under the theme “Structure and Evolution of the Universe.” G.W. is supported by a National Research Administration fellowship. K.C. is supported by a Graduate Student Researcher Program fellowship.

REFERENCES

- Bennett, C. L. *et al.* 1996, ApJ, **464**, L1.
- Bond, J. 1994, Phys. Rev. Lett., **74**, 4369.
- Bond, J. R., Jaffe, A., and Knox, L. 1998a, Phys. Rev. D, **57**, 2117.
- Bond, J. R., Jaffe, A., and Knox, L. 1998b. Submitted to ApJ. preprint astro-ph/9808264.
- Bond, J. R. and Jaffe, A. H. 1997. Cosmic Parameter Estimation Combining Sub-Degree CMB Experiments with COBE. In *Microwave Background Anisotropies*, Proceedings of the 31st Moriond meeting. in press, preprint astro-ph/9610091.
- Bunn, E. F., Hoffman, Y., and Silk, J. 1995. astro-ph/9509045.
- Bunn, E. F. and White, M. 1997, ApJ, **480**, 6.
- Cheng, E. S. *et al.* 1996, ApJ, **456**, L71.
- Cheng, E. S. *et al.* 1997, ApJ.
- Cheng, E. S. *et al.* 1994, ApJ, **422**, L37.
- Fixsen, D. J. *et al.* 1996, ApJ, **470**, 63.
- Goldin, A. B. *et al.* 1997, ApJ, **488**.
- Inman, C. A. *et al.* 1997, ApJ, **478**, L1.
- Knox, L. 1999. preprint astro-ph/9902XXX.
- Knox, L., Bond, J., Jaffe, A., Segal, M., and Charbonneau, D. 1998, Phys. Rev. D, **58**, 083004.
- Netterfield, C. B., Devlin, M. J., Jarosik, N., Page, L., and Wollack, E. J. 1997, ApJ, **474**, 47.
- Oh, S., Spergel, D., and Hinshaw, G. 1999, ApJ. submitted.
- Rudy, D. J., Muhleman, D. O., Berge, G. L., Jakosky, B. M., and Christensen, P. R. 1987, Icarus, **71**, 159.
- Tegmark, M. 1998. preprint astro-ph/9802123.
- Tegmark, M., de Oliveira-Costa, A., Devlin, M., Netterfield, C., Page, L., and Wollack, E. 1997, ApJ.
- Tegmark, M., Taylor, A., and Heavens, A. 1996, ApJ.